

# Aging characteristics of lithium-ion battery under fast charging based on electrochemical-thermal-mechanical coupling model

Dongxu Zuo and Peichao Li \*

School of Mechanical and Automotive Engineering  
Shanghai University of Engineering Science  
Longteng Road 333, Shanghai 201620, PR China  
[wiselee18@163.com](mailto:wiselee18@163.com)

**Keywords:** lithium-ion battery • aging characteristics • fast charging • electrochemical-thermal-mechanical coupling model

**Abstract:** This paper numerically investigates the aging characteristics of lithium-ion battery (LIB) under fast charging based on an electrochemical-thermal-mechanical (ETM) coupling model. First, the ETM coupling model is established and solved by COMSOL Multiphysics. Subsequently, a long cycle test is conducted to explore the aging characteristics of LIB. Specifically, the effects of increasing C rates and number of cycles on battery aging are analyzed in terms of non-uniform distribution of solid electrolyte interface (SEI), SEI formation, thermal stability and stress characteristics. The results indicate that the increase in C rates and cycling leads to an increase in the degree of non-uniform distribution of SEI, as well as a consequent increase in the capacity loss due to SEI formation. Meanwhile, the increase in C rates and the number of cycles also led to an increase in the heat generation and a decrease in the heat dissipation rate of the battery, respectively, which result in a decrease in the thermal stability of the electrode materials. In addition, the von Mises stress of the positive electrode material is higher than that of the negative electrode material as the cycling proceeds, with the positive electrode material exhibiting tensile deformation and the negative electrode material exhibiting compressive deformation. The available lithium ion concentration of the positive electrode is lower than that of the negative electrode, proving that the tensile-type fracture occurring in the positive material under long cycling dominated the capacity loss process. The aforementioned studies are helpful for researchers to further explore the aging behavior of LIB under fast charging and take corresponding preventive measures.

## 1. Introduction

In an environment of global warming and energy scarcity, the energy landscape is evolving towards sustainability, green and energy efficiency [1,2]. Among various clean energy sources, lithium-ion batteries (LIBs) stand out for their high energy density, light weight and long life [3,4]. Nowadays, it has experienced decades of dynamic development and is widely

used in electronics, electric vehicles and energy storage products [5,6]. The consequent increase in demand for performance has further contributed to a significant increase in the energy density of LIBs, which can lead to a number of safety issues [7-10].

The most significant issue that occurs in LIBs over extended periods is aging, especially under fast charging (high C rates), which includes both capacity and energy density fade [11-13]. The aging phenomenon includes the deformation of battery materials, the loss of available lithium ions, and the reduction of thermal stability [14-16]. Consequently, it is critical to focus on and understand the aging behavior of LIB under fast charging.

In general, model-based research on the mechanism description of LIBs is currently conducted through electrochemical models, and most of them are based on the Pseudo-2D (P2D) model developed by Newman et al. [17-18]. On the basis of the P2D model, many researchers have established electrochemical-thermal (ET) coupling model of LIBs by incorporating different heat generation mechanisms. For example, Ren et al. [19] developed an ET coupling model for square batteries to simulate the thermal behavior during battery discharge. The simulation results showed that the heat distribution of porous electrode is not uniform and the heat generation increases with the increase of discharge rates. He et al. [20] investigated the thermal behavior of  $\text{LiFePO}_4$  cells under natural convection conditions and different C rates (1C, 3C, and 5C) based on a three-dimensional ET coupling model. The numerical results showed that the average particle size of the electrodes directly affects the heat generation rate during the discharge process. The uneven distribution of local currents will lead to uneven distribution of heat generation rate, which in turn will lead to uneven distribution of battery temperature. In addition to the effects of temperature, some researchers have also incorporated stress fields into their models to study the

1 effects of stress on battery behavior. Zhang et al [21]  
 2 investigated the diffusion-induced stresses (DIS) in  $\text{LiMn}_2\text{O}_4$   
 3 ellipsoidal active particles. The results of the simulation  
 4 indicated that larger aspect ratios and smaller sized ellipsoidal  
 5 particles can reduce the stresses generated by lithiation. Wu  
 6 and Lu [22] developed an electrochemical-mechanical coupling  
 7 model to predict the intercalation-induced stresses in secondary  
 8 particles with agglomerated structures. It has been shown that  
 9 the dependence of the open-circuit voltage of the active material  
 10 on the lithium ion concentration decreases the stress level. At  
 11 the same time, the higher the surface overpotential amplitude of  
 12 the secondary particles, the higher the stress level.

13 The study of aging behavior of LIBs based on the  
 14 electrochemical model has also been extensively reported by  
 15 many researchers. Ouyang et al. [23] performed long-term  
 16 cycling of three battery samples with 90% state of health (SOH)  
 17 under different C rates to explore their electrochemical features  
 18 and thermal behaviors. It is demonstrated that the thermal  
 19 stability of both electrode materials is decreased due to the  
 20 electrolyte decomposition and the gradual accentuation of  
 21 lithium deposition on the surface of the electrode materials  
 22 under the long cycle. This further worsens the thermal runaway  
 23 behavior of the battery during overheating and the severity  
 24 aggravates as the C rate increases. Sun et al. [24] used  
 25 ultrasonic technology to detect the mechanical evolution inside  
 26 the battery after long cycling by analyzing the changes of  
 27 acoustic waves. The nonlinear fade trajectory of the battery is  
 28 revealed, and it is shown that it is the collapse of the positive  
 29 electrode material that dominated the capacity loss of the battery  
 30 under high-rate discharging conditions. Zhang et al. [25]  
 31 illustrated the complex mechanism of thermal evolution of LIBs  
 32 at high temperatures by analyzing from multiple perspectives. It  
 33 is shown that lithium plating contributes to the reduction of the  
 34 self-heating initial temperature and that the gas produced by the  
 35 reaction leads to a reduction in the temperature of the thermal  
 36 runaway trigger. In addition, the loss of active material and  
 37 available lithium ions during aging results in a decrease in  
 38 maximum temperature and temperature rise rate, indicating a  
 39 reduction in the thermal hazard of aging battery. S. Yang et al.  
 40 [26] investigated the aging phenomenon of the separators during  
 41 battery cycling and found that the degradation products of  
 42 electrolyte and graphite appeared on the surface of the  
 43 separators as the number of cycles increased. This in turn leads  
 44 to a decrease in porosity and an increase in ionic conductivity  
 45 and internal resistance of the separators. Finally, with the  
 46 increase of the current rate and the number of cycles, the  
 47 mechanical properties of the separators gradually deteriorate.

The aforementioned studies have extensively investigated  
 the electrochemical features, thermal behavior, and even the  
 mechanical characteristics of separators. However, there has  
 been a limited focus on the specific analysis from the  
 perspective of multi-physical field coupling. This limitation makes  
 it challenging to comprehend the mechanism through the lens of  
 the electrochemical reaction mechanism. Furthermore, in recent  
 years, the pursuit of enhanced battery charging speed has often  
 led to the adoption of fast charging strategies such as high  
 current rates. Generally, the aging behavior of the battery may  
 vary under different C rates.

In view of this, this paper investigates the aging behavior of  
 batteries by using an ETM coupling model under fast charging.  
 Because the ETM coupling model effectively illustrates the  
 interconnected mechanisms across various physical fields, and  
 furthermore can reveal the principle of the phenomenon. Here,  
 the fast charging condition is considered to be high C rate  
 constant current charging (3C, 4C and 5C) condition. On the  
 basis of the established model, the electrochemical  
 characteristics under different C rates, with a specific focus on  
 characterizing SEI formation under high C rates will be analyzed  
 in this paper. The change of thermal stability of electrode  
 material after long cycle is also analyzed. Lastly, the causes of  
 mechanical damage of electrode material after the long-term  
 cycling is discussed. This work aims to provide valuable insights  
 for researchers to investigate the root causes of aging and  
 formulate corresponding protective measures to mitigate aging  
 effects.

## 2. Theory/calculation

In the previous group's works [27-29], a Pseudo-3D (P3D)  
 model was developed based on the P2D model created by  
 Newman, Doyle et al. [17-18] which can more accurately  
 describe the reaction mechanism within the battery. The  
 geometry model is shown in Fig. 1.

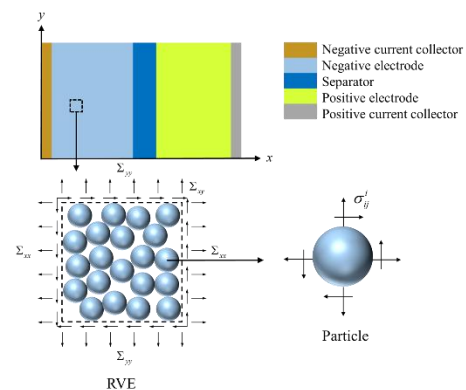


Figure 1. Schematic of P3D geometric model

### 2.1. De-/intercalation reaction

The governing equations related to the theory of porous electrodes and concentrated solutions have been described in detail in a large number of literatures. [27-32] So that we focus on the model extensions with regard to the side reactions.

The current density  $i_n$  of the lithium de-/intercalation reaction is calculated by the Butler-Volmer equation.

$$i_n = i_{0,n} \left( \exp\left(\frac{\alpha_a F \eta}{RT}\right) - \exp\left(\frac{-\alpha_c F \eta}{RT}\right) \right) \quad (1)$$

$$i_{0,n} = F k c_{s,surf}^{\alpha_c} c_l^{\alpha_a} (c_{s,max} - c_{s,surf})^{\alpha_a} \quad (2)$$

where  $\alpha_a$  and  $\alpha_c$  are the charge transfer coefficients at the negative electrode and the positive electrode,  $R$ ,  $T$  and  $F$  are the universal gas constant, the absolute temperature and the Faraday's constant, respectively.  $i_{0,n}$  is the exchange current density,  $k$  is the reaction rate constant.  $c_{s,surf}$  and  $c_{s,max}$  are the lithium-ion concentrations at the particle surface and the maximum concentration of lithium concentrations.  $\eta$  is the electrode overpotentials,  $c_l$  is the electrolyte concentrations.

In the ETM coupling model, considering the effects of temperature and stress as well as surface resistance due to SEI growth on the overpotential, the corrected equations are as follows [30]:

$$\eta = \phi_s - \phi_e - E_{eq} - i_{F,SEI} R_{film} \quad (3)$$

$$E_{eq} = E_{ref} + (T - T_{ref}) \frac{\partial E_{eq,i}}{\partial T} + \frac{\Omega \sigma_h}{F} \quad (4)$$

where  $\phi_s$ ,  $\phi_e$  are the electrode potential, the electrolyte potential, respectively.  $E_{eq}$  is the open circuit potential.  $i_{F,SEI} R_{film}$  is caused by surface resistance of the side reaction product film.  $E_{ref}$  is the open circuit potential due to the diffusion of lithium concentration,  $(T - T_{ref}) \frac{\partial E_{eq,i}}{\partial T}$  and  $\frac{\Omega \sigma_h}{F}$  represent the extra potential induced by the temperature gradient and the hydrostatic stress, respectively.  $T_{ref}$  is the reference temperature.

### 2.2. SEI formation

In this work, SEI is considered to be an electrochemical reduction product of the electrolyte. The product precipitates on the surface of the negative graphite particles to form a SEI. The reaction current for SEI follows B-V kinetics with concentration and temperature dependence and is expressed as [31]

$$i_{F,SEI} = -n F K_{SEI} C_O^{(1-\alpha)} C_R^\alpha \frac{C_l}{C_{l,0}} \exp\left(\frac{-0.5 F \eta}{RT}\right) \quad (5)$$

where  $K_{SEI}$  is the SEI reaction rate constant,  $C_o$  is the oxide concentration,  $C_R$  is the reductant concentration, and  $C_{l,0}$  is the liquid initial concentration.

Because the long-cycle test is performed under fast charging, and taking into account the effect of C rate on  $K_{SEI}$ , the  $K_{SEI}$  is corrected to be [31]

$$K_{SEI} = k_{SEI} \cdot \exp\left(-\frac{E_{a,SEI}}{RT}\right) \cdot \frac{i_{loc}}{i_{1C,loc,neg}} \quad (6)$$

$$i_{1C,loc,neg} = \frac{-i_C}{S_{a,neg} L_{neg}} \quad (7)$$

where  $i_{loc}$  is the local current density,  $i_{1C,loc,neg}$  is the local current density of the negative electrode under 1C.  $S_{a,neg}$  is the specific surface area of the negative electrode, and  $L_{neg}$  is the length of the negative electrode.

The capacity loss due to SEI formation is calculated using the concentration of SEI with the equation [32]

$$\frac{dc_{SEI}}{dt} = \frac{-i_{SEI} S_{a,neg}}{F} \quad (8)$$

$$C_{loss} = \frac{c_{SEI}}{c_{s,max,neg} SOC_0} C_0 \quad (9)$$

where  $C_{loss}$  is the lost capacity,  $c_{s,max,neg}$  is the initial maximum concentration of the negative solid phase,  $SOC_0$  is the initial state-of-charge (SOC), and  $C_0$  is the initial capacity of the battery.

### 2.3. Heat transfer model

During the operation of LIBs, the heat generated by the battery is divided into three parts: the activation polarization heat ( $Q_{act}$ ), the ohmic heat ( $Q_{ohm}$ ) and the reaction heat ( $Q_{rea}$ ). The heat transfer model can be described by the law of conservation of energy [33-34].

$$\rho_i C_{p,i} \frac{\partial T}{\partial t} + \nabla \cdot (-\lambda \nabla T) = Q_{act} + Q_{rea} + Q_{ohm} \quad (10)$$

where  $\rho_i$ ,  $C_{p,i}$ ,  $\lambda$  are the battery material density, the specific heat capacity and the thermal conductivity, respectively.

The  $Q_{act}$ ,  $Q_{ohm}$  and  $Q_{rea}$  are calculated using the following equations, respectively [33-34].

$$Q_{rea} = S_a i_F T \frac{dE_{eq,ref}}{dT} \quad (11)$$

$$Q_{act} = S_a i_F (\phi_s - \phi_e - E_{eq}) \quad (12)$$

$$Q_{ohm} = \sigma_s^{eff} \nabla \phi_s^2 + \sigma_e^{eff} \left( \nabla \phi_e^2 + \frac{2RT}{F} \left( 1 + \frac{\partial \ln f}{\partial \ln c_e} \right) (1-t_+) \nabla c_e \nabla \phi_e \right) \quad (13)$$

1 In this work, the heat exchange between the battery and  
 2 external environment is regarded as a heat conduction process.  
 3 The boundary conditions governing this exchange are described  
 4 by the Newton's law of cooling:

$$-\lambda \nabla T = h (T - T_{amb}) \quad (14)$$

5 where  $h$  is the effective surface heat transfer coefficient of the  
 6 battery, and  $T_{amb}$  is the ambient temperature around the battery.  
 7

#### 8 2.4. Solid mechanics model

9 Because the constructed model is a P3D model, both  
 10 particle-scale and electrode-scale stresses and strains can be  
 11 considered. On the particle scale, the radial and tangential  
 12 strains inside the isotropic spherical particles are described as  
 13 follows [28,35]

$$\varepsilon_{rr}^* = \frac{1}{E_p} (\sigma_{rr}^* - 2\nu_p \sigma_{\theta\theta}^*) + \frac{\Omega}{3} \Delta c + \alpha \Delta T \quad (15)$$

$$\varepsilon_{\theta\theta}^* = \frac{1}{E_p} (\sigma_{\theta\theta}^* - \nu_p (\sigma_{\theta\theta}^* + \sigma_{rr}^*)) + \frac{\Omega}{3} \Delta c + \alpha \Delta T \quad (16)$$

14 where  $E_p$ ,  $\nu_p$  and  $\alpha$  are the Young's modulus, the Poisson's  
 15 ratio and the coefficient of thermal expansion of the particle,  
 16 respectively. The superscript \* indicates particle scale.

17 The electrode scale takes into account the stresses induced  
 18 by the lithium ions concentration gradient and the temperature  
 19 gradient, so that the intrinsic equation of the electrode is

$$\varepsilon = \frac{1}{E} ((1+\nu) \sum_{ij} - \nu \sum_{kk} \delta_{ij}) + \frac{\Omega}{3} \Delta c \delta_{ij} + \alpha \Delta T \delta_{ij} \quad (17)$$

20 where  $\sum_{ij}$ ,  $\delta_{ij}$  are the electrode level stress and the Dirac delta  
 21 function, respectively.

22 The hydrostatic stress induced by the lithium ions  
 23 concentration gradient is

$$\sigma_h^*(r) = \frac{\sigma_{rr}^* + 2\sigma_{\theta\theta}^*}{3} = \frac{2\Omega E_p}{3(1-\nu_p)} \left( \frac{1}{r_p^3} \int_0^{r_p} \Delta c r^2 dr - \frac{\Delta c}{3} \right) \quad (18)$$

24 The hydrostatic stress between electrode layers is  
 25 calculated based on volume average theory.

$$\sigma_h^i = \frac{\sigma_{xx}^i + \sigma_{yy}^i + \sigma_{zz}^i}{3} = \frac{\sum_{xx} + \sum_{yy} + \sum_{zz}}{3\varepsilon_s} \quad (19)$$

26 The total hydrostatic stress can be obtained by combining  
 27 Eq. 18 and Eq. 19 to solve.

$$\sigma_h = \sigma_h^* + \sigma_h^i \quad (20)$$

#### 2.5. Model validation

In this work, the ETM coupling model is solved by COMSOL Multiphysics. First, a mesh-independent analysis is performed. Two meshing methods are chosen and the results are shown in Fig. 2A and Fig. 2B. The mesh density of mesh 1 is much smaller than that of mesh 2. The results of the model with the two mesh densities are shown in Fig. 3. Fig. 3 shows the variation of the voltage and von Mises stress with time under different C rates. The lines represent mesh 1 and the symbols represent mesh 2. The results show that the symbols and lines match very well, which indicates that the mesh density has little effect on our modeling results. However, different mesh densities have a significant effect on the time required for computation, so a medium density of meshing was chosen for this study. The final mesh calculated in this work is shown in Fig. 2C.

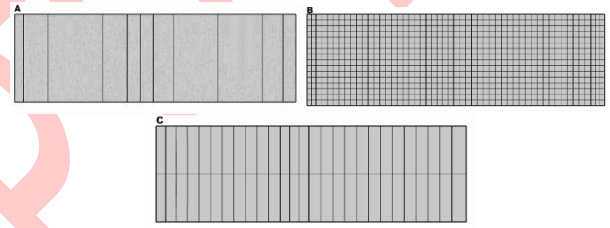
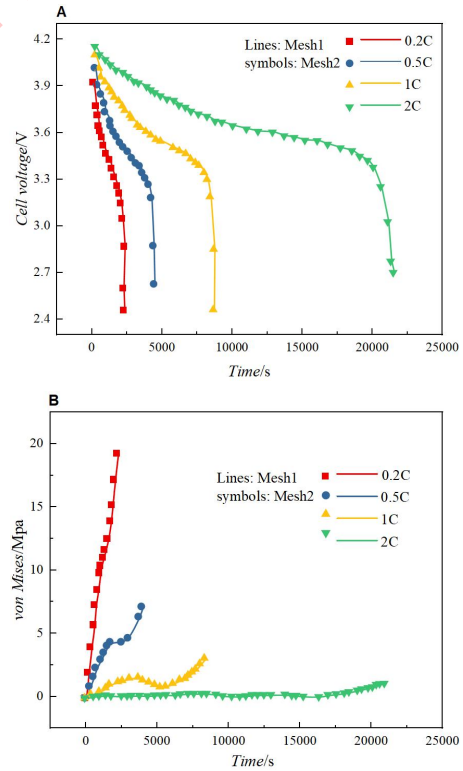


Figure 2. Different mesh density.



1 **Figure 3.** Voltage (A) and von Mises stress (B) variation over time under  
 2 different C rates.

3  
 4 The ETM coupling model is compared with the experimental  
 5 data of Keil and Jossen [36] to verify the accuracy and  
 6 applicability of the model. The boundary conditions are  
 7 prescribed in accordance with the experiment. Keil and Jossen  
 8 conducted the test using commercial graphite battery with a  
 9 standard capacity of 2.05 Ah, table 1 gives the specific  
 10 parameters of the battery to be used. The boundary conditions  
 11 are prescribed in accordance with the experiment. In the  
 12 simulation, the initial ambient temperature is set as 25 °C, and  
 13 the voltage variation curves and temperature variation curves

are verified at different discharge rates (0.1C, 0.2C, 0.5C, 1C  
 and 2C), respectively. And the capacity fade is verified under 1C.  
 As shown in Fig. 4, the solid line represents the simulation data,  
 and the points represent the experimental data. It is evident that  
 the simulation results closely align with the experimental data,  
 thereby confirming the model's accuracy. It is worth noting that  
 Keil and Jossen's study only considered the effect of the  
 temperature field on the electrochemical field and neglected the  
 effect of the stress field. In contrast, we use the ETM coupling  
 model so that the effects of both the temperature and stress  
 fields can be considered, which will be discussed in detail later.

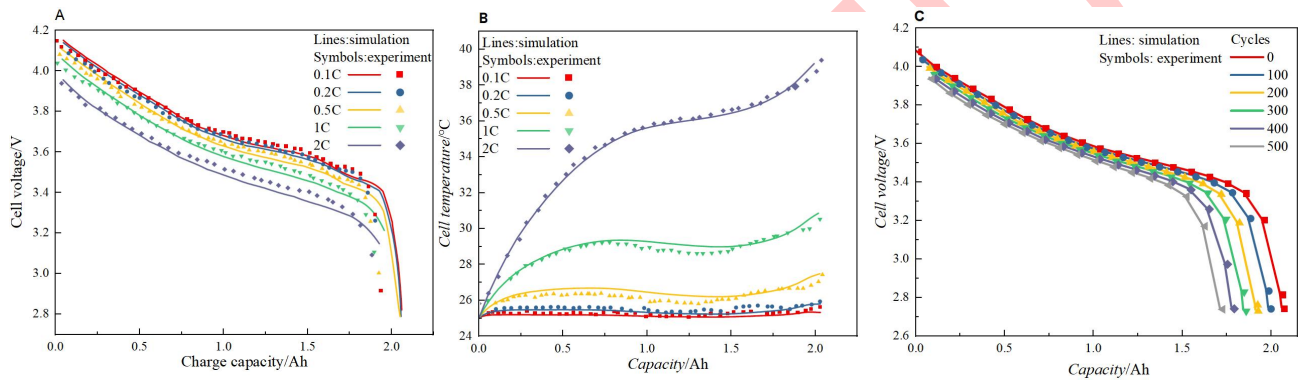


**Figure 4.** Comparison of simulation results and experimental data under different discharge rates. (A) Voltage (B) Surface temperature (C) Capacity loss.

**Table 1** Parameters of NCM battery used in the ETM coupling model.

Parameters	Unit	Negative electrode	Separator	Positive electrode
Thickness $l$	$\mu\text{m}$	70	20	60
Mean particle radius $r_p$	$\mu\text{m}$	10		4
Solid phase fraction $\varepsilon_s$		0.59		0.61
Liquid phase fraction $\varepsilon_l$		0.3	0.45	0.3
Maximum $\text{Li}^+$ concentration $c_{s,\text{max}}$	$\text{mol} \cdot \text{m}^{-3}$	31370		51385
Initial $\text{Li}^+$ concentration $c_{s,\text{surf}}$	$\text{mol} \cdot \text{m}^{-3}$	25086		20544
Initial $\text{Li}^+$ concentration $c_l$	$\text{mol} \cdot \text{m}^{-3}$		1000	
Initial state of charge $\text{SOC}_0$		0.8		0.4
Anodic charge-transfer coefficient $\alpha_a$		0.5		0.5
Cathodic charge-transfer coefficient $\alpha_c$		0.5		0.5
Reaction rate constant $k$	$\text{m} \cdot \text{s}^{-1}$	$1.5 \times 10^{-11}$		$1.5 \times 10^{-11}$
Universal gas constant $R$	$\text{J} \cdot \text{mol}^{-1} \cdot \text{K}$	8.314	8.314	8.314
Faraday's constant $F$	$\text{C} \cdot \text{mol}^{-1}$	96485	96485	96485
Transport number $t_+$			0.38	
Reaction rate constant for SEI formation $K_{\text{SEI}}$	$\text{m} \cdot \text{s}^{-1}$	$K_{\text{SEI}} = 9.85 \times 10^{-4} \times \exp\left(\frac{-15700[\text{J/mol}]}{RT}\right)$		
Battery material density $\rho_i$	$\text{kg} \cdot \text{m}^{-3}$	1555	1017	2895
Specific heat capacity $C_{p,i}$	$\text{J} \cdot \text{kg}^{-1} \cdot \text{K}^{-1}$	1437	1978	1270
Thermal conductivity $\lambda$	$\text{W} \cdot \text{m}^{-1} \cdot \text{K}^{-1}$	1.04	0.34	1.58
Reference temperature $T_{\text{amb}}$	K	298	298	298

Young's modulus $E_p$	12	0.25	10
Poisson's ratio $\nu_p$	0.3	0.35	0.3
Coefficient of thermal expansion $\alpha$	$4.06 \times 10^{-6}$	$1.3 \times 10^{-4}$	$8.62 \times 10^{-6}$

### 3. Results and Discussion

This section begins with a long cycle simulation test of the battery using COMSOL Multiphysics. The battery is a Sanyo NCM battery with a capacity of 2.05Ah, the ambient temperature is 25°C, and the charging and discharging sequence is discharge

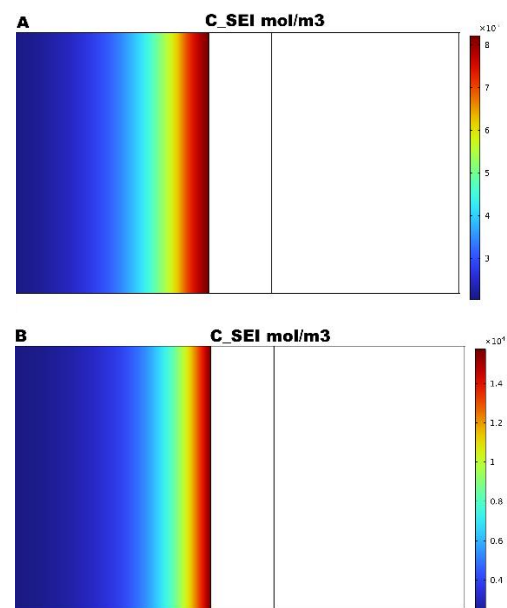
first then charge. Then the aging characteristics of the battery are discussed. Specifically, the non-uniform distribution of SEI in space and the growth difference under different C rates are analyzed. The thermal behavior of the battery under long cycles is further explored, and it is proved that the heat dissipation performance of the battery material gradually deteriorates with the increase of the number of cycles. Finally, the stress behavior of the battery is discussed, which is changing all the time during the charging and discharging process. Compared to the negative electrode, the tensile type fracture of the positive electrode material dominates the capacity loss process of the battery.

#### 3.1. Non-uniform distribution of SEI

As introduced earlier, SEI formation predominantly occurs during the charging process. While lithium ions migrate from the positive electrode to the negative electrode, they react with organic components in the electrolyte, forming a passivation film that covers the surface of the negative electrode. However, due to the gradient distribution of lithium ions concentration in the cell, the generated SEI exhibits a non-uniform distribution. As shown in Fig. 5, the SEI distribution is investigated over 500 cycles under 1C rate. As can be observed from Fig. 5, it is evident that the SEI concentration shows a non-uniform pattern across the entire region from the negative electrode to the separator. Moreover, the closer a region is to the separator, the higher the concentration of SEI. This is due to the higher concentration of lithium ions at the interface between the negative electrode and the separator compared to the side near the negative electrode, resulting in a high concentration of SEI. The nonuniformity of the SEI distribution is subsequently analyzed under 2C and 3C rates, respectively, revealing that the concentration of SEI generation gradually increased with the increase of C rate. This phenomenon can be attributed to the fact that, as indicated by Equations 5-8, the reaction rate of SEI formation increases with the elevated current rate. Consequently, there is an associated increase in the current density of SEI formation, ultimately manifesting as a heightened concentration

of SEI. Essentially, an elevation in the C rate not only accelerates the reaction rate of the side reaction but also augments the formation of SEI. As a result, the capacity loss of the battery becomes more pronounced.

After analyzing the nonuniformity of the SEI distribution under different C rates, the distribution of the SEI is explored at the end cycles of 100, 200, 300, 400, and 500, respectively. As depicted in Fig. 6A, the concentration of SEI gradually increased with the increase of the number of cycles. This observation is evident because, with an increase in the number of charging and discharging cycles, more lithium ions react with the organic components in the electrolyte, leading to a more pronounced lithium deposition phenomenon. Fig. 6B illustrates that the degree of non-uniformity in distribution across the negative domain also progressively increases with the charging and discharging rate. This phenomenon can be attributed to the inherent gradient distribution of lithium ions throughout the entire region from the negative electrode to the separator. The increase of the charging and discharging rate exacerbates the extent of this gradient distribution of lithium ions. It also accelerates the reaction rate of SEI formation. This suggests that the capacity loss of battery resulting from SEI formation becomes increasingly prominent with a higher number of battery cycles. As depicted in Fig. 7, the capacity loss of the battery under various cycles is evident not only in the concentration of SEI generation but also in the degree of non-uniformity in spatial distribution.



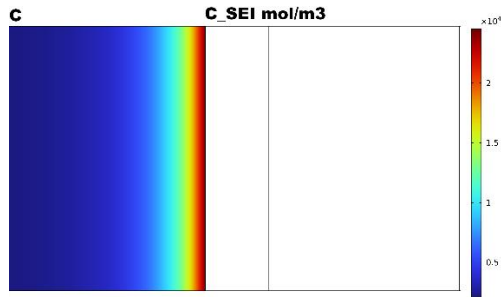


Figure 5. SEI distribution under different C rates at 500 cycles. (A: 1C, B: 2C, C: 3C)

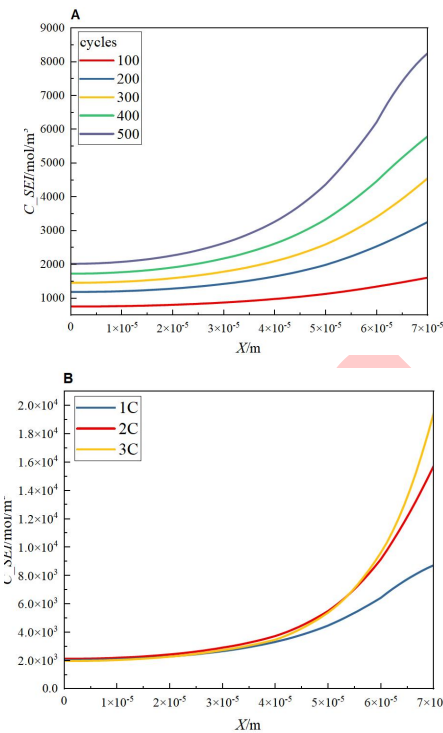


Figure 6. Distribution of SEI concentration. (A) Every 100 cycles under 1C. (B) 500 cycles under 1C, 2C and 3C.

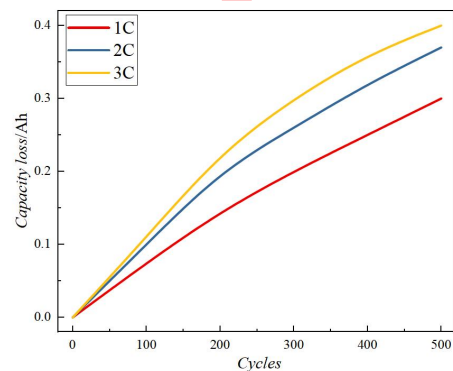
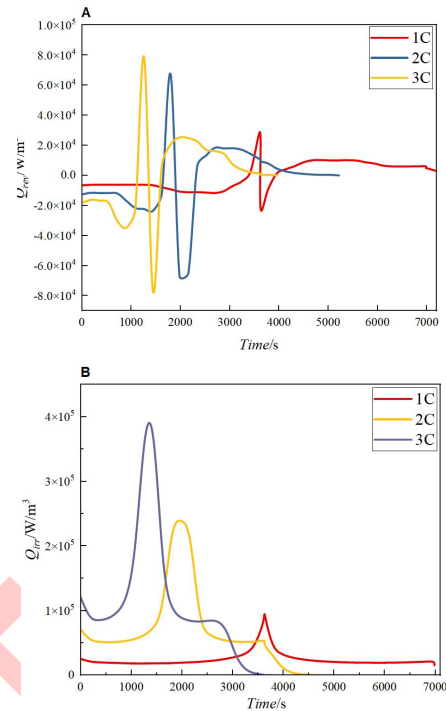
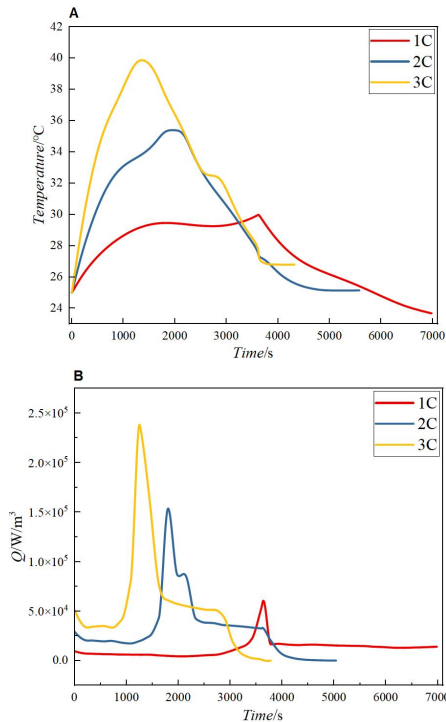


Figure 7. Capacity loss of the battery at different cycles under 1C, 2C and 3C.

### 3.2. Thermal behavior

As described by the heat source equation in the solid heat transfer field in the second subsection, the heat generation of LIBs during operation is divided into three main heat sources, which are activation polarization heat, the ohmic heat and the reaction heat. The process of exchanging heat between the battery and the external environment is considered a heat conduction process and is described by the Newton's law of cooling. Initially, the temperature variation over time under 1C, 2C, and 3C rate are investigated. As depicted in Fig. 8A, the temperature rapidly increases to its peak during the discharge phase and then decreases during the charging phase. This behavior stems from the fact that the batteries react more strongly during discharge compared to charge, resulting in a higher final temperature after discharge than after charge. Consequently, throughout the discharge-charge cycle, the temperature reaches its maximum point after discharge. According to the Newton's law of cooling, at this moment the temperature difference with the external environment is at its peak, and a strong heat conduction process with the external environment begins. According to Fig.8B, it can be obtained that the heat generation rate during charging is lower than that during discharging, resulting in less heat production than heat dissipation, which is ultimately manifested as a decrease in temperature. Furthermore, with an increase in the current rate, both the slope of the temperature curve and the maximum temperature value exhibit an increasing trend.

Then the variation in temperature rise under different C rates are examined by analyzing the heat generation rates. As shown in Fig. 9, the curves illustrating the reaction heat generation rate and ohmic heat generation rate with time under different rates are presented. With an increase in the C rate, the reaction heat generation rate begins to increase, although the difference between the various C rates is not particularly significant. In contrast, the ohmic heat generation rate exhibits a large difference, which is because according to the Joule's law, simply increasing the current causes the ohmic heat to increase exponentially. Thus, the difference in ohmic heat under different C rates is much more significant compared to that of the reaction heat. From the values of the final heat generation rate, the difference between the ohmic and reaction heat values is small only under 1C. As the C rates increases, the ohmic heat generation rate becomes considerably larger than that of the reaction heat. This also proved that the ohmic heat is the main heat source contribution during the charging and discharging process of the battery, which is also consistent with the report of Yea et al [37].



**Figure 8.** Temperature (A) and variation of total heat generation rate (B) over time under 1C, 2C and 3C rate.

**Figure 9.** Different parts of heat generation rate in LIB under different C rates. (A) Reversible heat. (B) Irreversible heat.

1 During the long cycling of the battery, thermal expansion  
 2 resulting from the increased internal resistance and heat  
 3 generation contributes to the aging of the electrode material,  
 4 manifested by the degradation of the thermal stability of the  
 5 electrode material. The previous paragraph has discussed the  
 6 heat generation rate and the temperature change of the battery  
 7 under different C rates. In this context, our analysis shifts to the  
 8 battery's heat dissipation characteristics. As shown in Fig. 10,  
 9 the distribution of heat flux on the negative electrode under  
 10 different C rates is presented at the end of 100 and 500 cycles,  
 11 respectively. Here, the heat flux is expressed as the magnitude  
 12 of heat passing through a unit area per unit time and is related to  
 13 the thermal conductivity and temperature change by the  
 14 equation  $\phi_q = k \nabla T$ . It can be obtained that the closer to the  
 15 separator, the higher the heat flux. This is due to the fact that the  
 16 closer the separator is to the more intense degree of reaction  
 17 leading to more heat generation, the temperature change is  
 18 significant and thus leads to an increase in heat flux. Fig. 10B  
 19 shows the heat flux on the negative electrode at the end of 500

cycles. It can be noted that the heat flux under different C rates  
 at 500 cycles is slightly lower compared to 100 cycles. This  
 means that the heat dissipation of the negative material at 500  
 cycles is much lower compared to 100 cycles because the heat  
 is gradually accumulated as the reaction proceeds. This  
 demonstrates that the thermal stability of the electrode material  
 decreases gradually during long battery cycling, as evidenced by  
 a decrease in the heat dissipation rate.

Subsequently, the same analysis is conducted for the heat  
 dissipation rate of the positive electrode material, as shown in  
 Fig. 11. Comparing the heat flux of the positive electrode at the  
 end of 100 and 500 cycles with that of the negative electrode  
 reveals consistent characteristics, which further verified the  
 aging of the battery material at the end of the cycle. However, it  
 is worth noting that in terms of the magnitude of heat flux, the  
 heat flux of the positive electrode is smaller than that of the  
 negative electrode. This implies that the positive material has  
 more severe aging of the electrode material after long cycling  
 compared to the negative material.

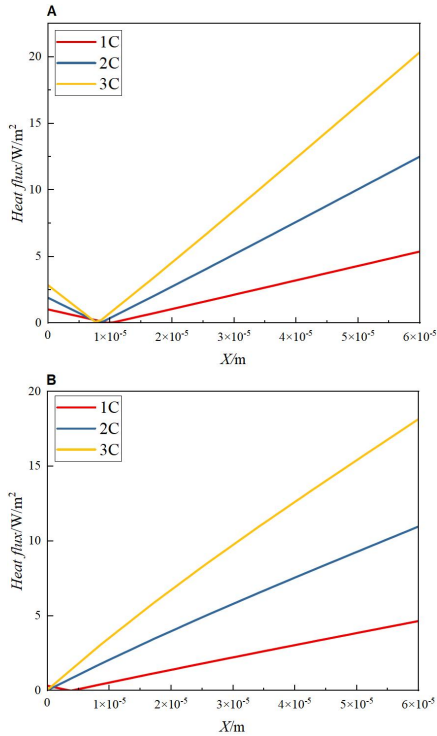


**Figure 10.** Heat flux on the negative electrode under different C rates at the end of different cycles. (A) 100 cycles (B) 500 cycles.

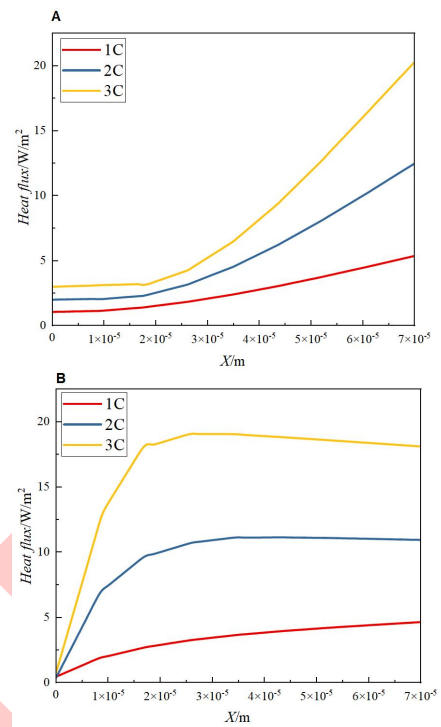


**Figure 11.** Heat flux on the positive electrode under different C rates at the end of different cycles. (A) 100 cycles (B) 500 cycles.

1 3.3. Stress behavior

2 During the operating process of LIBs, the DIS caused by  
 3 repeated de-embedding of lithium ions and thermal expansion  
 4 caused by temperature changes will cause corresponding  
 5 mechanical damage to the battery. The DIS of the LIB is first  
 6 analyzed under 5C rate. Specifically, on the particle scale,  
 7 during the discharge process, the radial stresses inside the  
 8 spherical particles are in compression as shown in Fig. 12. The  
 9 compressive radial stress is highest at the center and  
 10 decreases monotonically to 0 on the particle surface under 5C  
 11 rate during the discharge process. Similarly, Fig. 12B shows the  
 12 tangential component of the DIS in the negative particles during

the discharge process. As the discharge progress, the  
 tangential stresses are compressive at the center of the  
 spherical particle and tensile on the surface. At the particle's  
 center, the tangential and radial stresses are consistently equal,  
 resulting in a stress state that is entirely hydrostatic. The  
 transition from compression to tension occurs at  $r = 1/\sqrt{2}$   
 after the stress reaches steady state. Then, the von Mises  
 stress on the particle surface is discussed, as depicted in Fig.  
 12C. Throughout the discharge process, the von Mises stress is  
 0 at the center of the particle and reaches a maximum at the  
 surface of the spherical particles, with stress values varying at  
 different time points.

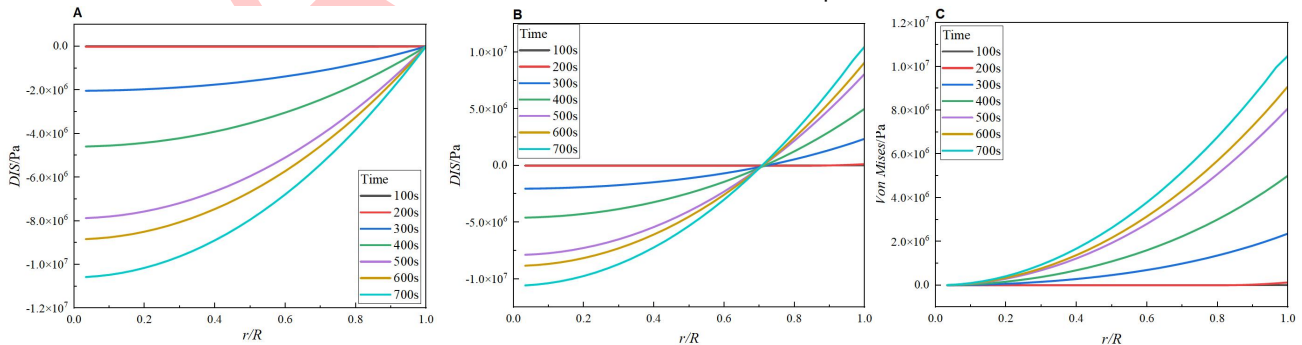


**Figure 12.** DIS at different moments under 5C rate. (A) Radial component of induced stress (B) Tangential component (C) Von Mises stress.

1 Furthermore, the von Mises stress on the positive and  
 2 negative electrodes are analyzed at the end of discharge under  
 3 different cycles. As shown in Fig. 13A, the von Mises stress on

both the positive and negative electrodes exhibit an increasing  
 trend with the number of cycles, with the stresses on the positive  
 electrode surpassing those on the negative electrode. This

1 indicates that the DIS is more active on the positive electrode  
 2 during long cycles and may have a more severe effect on the  
 3 positive material.

4 Later, the available lithium ions concentration at the positive  
 5 and negative electrodes at the end of different cycles during the  
 6 discharge process are compared under different cycles, as  
 7 shown in Fig. 13B. At the end of the initial discharge, the positive  
 8 electrode has the highest available lithium ions concentration, as  
 9 all lithium ions are embedded in the positive electrode, while the  
 10 lithium ions concentration in the negative electrode is 0. With the  
 11 progress of charge and discharge, the available lithium ions  
 12 concentration in the positive and negative electrodes gradually  
 13 decreases. However, after a long cycle, the available lithium  
 14 ions concentration of the positive electrode is less than that of  
 15 the negative electrode. This discrepancy implies that, after long  
 16 cycling, the positive material can receive fewer lithium ions than  
 17 the negative material can release. In essence, this suggests that  
 18 the aging of the positive material after extended cycling is more  
 19 pronounced than that of the negative material.

20 After long cycling, the electrode material will deform due to  
 21 repeated de-embedding of lithium ions. As illustrated in Fig. 14,  
 22 after 500 cycles, the surface of the negative electrode material  
 23 exhibited compressive deformation at the end of the discharge,  
 24 while the surface of the positive electrode material displayed  
 25 tensile deformation. And with the increase of the number of  
 26 cycles, the deformation becomes more serious. According to the  
 27 work of Sun et al. [18], the tensile-type fracture of the positive  
 28 material dominates the aging process of LIBs after long cycling.  
 29 Combined with the previous comparison of the von Mises stress  
 30 and available lithium ions concentration on positive and negative  
 31 electrode materials after long cycle, this is also confirmed in this  
 32 paper.

33

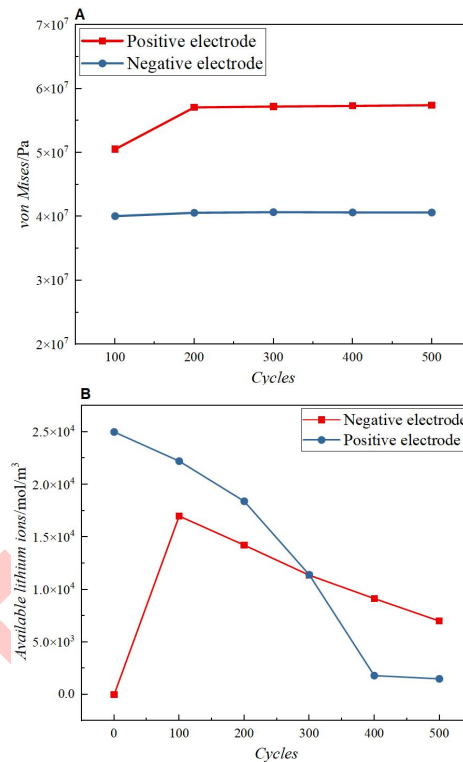


Figure 13. The von Mises stresses and the available lithium ions concentration at different cycles of under 3C rate.

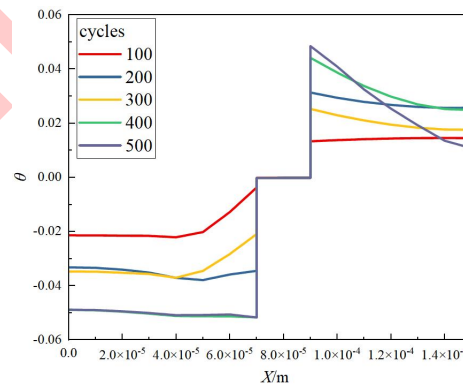


Figure 14. The volumetric strain of positive and negative electrode surface.

## 4. Conclusion

In this paper, the aging behavior of LIB under fast charging is investigated based on an ETM coupling model. The distribution of SEI, SEI formation, thermal stability and stress characteristics of the battery under different C rates and number of cycles are analyzed. The conclusions can be summarized as follows:

- (1) As the C rates increases, the non-uniformity of the SEI distribution due to the higher reaction current becomes more worse, and the concentration of SEI increases,

ultimately leading to a larger capacity loss of the battery after a long cycle.

(2) Due to the increase of C rates, the heat generation of the battery increases, and the temperature rise during the whole cycle is higher. At the same time, with the increase of the cycle numbers, the heat dissipation rate of the electrode material gradually decreases, which ultimately leads to the reduction of the thermal stability of the electrode material. And the degree of deterioration of the positive electrode material is worse than that of the negative electrode material.

(3) After long cycles, the von Mises stress of the positive electrode material is higher than that of the negative electrode material. Due to the distribution characteristics of DIS, the positive electrode material eventually exhibits tensile deformation and the negative electrode material exhibits compressive deformation. The temperature rise and stress changes under long cycling make the available lithium ion concentration in the positive electrode material lower than in the negative electrode material. It is finally demonstrated that the collapse of the positive electrode material dominates the capacity loss process of LIB under long cycling.

For simplicity, this study only considered the aging phenomenon of the battery under 500 cycles. However, in practical battery applications, lithium plating occurs in batteries after long cycles. In addition, the internal temperature distribution of cylindrical batteries is not uniform due to their layered structure. Therefore, the above points need to be further studied. The authors plan to complete the model with lithium plating and layered structure in the near future.

## Acknowledgements

This work was funded by the National Natural Science Foundation of China (Grant No. 12272217).

## References

- [1] Dong H, Liu Y, Zhao Z, Tan X, Managi S. Carbon neutrality commitment for China: from vision to action[J]. *Sustain. Sci.*, 2022, 17, 1741–1755.
- [2] Feng J, Yan J, Yu Z, Zeng X, Xu W. Case study of an industrial park toward zero carbon emission[J]. *Appl. Energy*, 2018, 209, 65–78.
- [3] Zubi L G., DufoLópez R., Carvalho M., Pasaoglu G. The lithium-ion cell: state of the art and future perspectives[J]. *Renew. Sust. Energ. Rev.*, 2018, 89, 292–308.
- [4] Lisbona D., Snee T. Process. Saf. A review of hazards associated with primary lithium and lithium-ion batteries[J]. *Environ. Prot.*, 2011, 6(89), 434–442.
- [5] Zhang G, Wei X, Han G, Dai H, Zhu J, Wang X, Tang X, Ye J. Lithium plating on the anode for lithium-ion batteries during long-term low temperature cycling[J]. *J. Power Sources*, 2011, 484, 229312.
- [6] You H, Zhu J., Wang X, Jiang B, Sun H, Liu X, Wei X, Han G, Ding S, Yu H, Li W, Sauer D U, Dai H. Nonlinear health evaluation for lithium-ion battery within full-lifespan[J]. *J. Energy Chem.*, 2022, 72, 333–341.
- [7] Nam G W, Park N Y, Park K J., Yang J., Liu J., Yoon C S, Sun Y K. Capacity Fading of Ni-Rich NCA Cathodes: Effect of Microcracking Extent[J]. *ACS Energy Lett.*, 2019, 4, 2995–3001.
- [8] Noh H J, Youn S., Yoon C S, Guo C S. Comparison of the structural and electrochemical properties of layered Li [Ni<sub>x</sub>CoyMnz] O<sub>2</sub> (x = 1/3, 0.5, 0.6, 0.7, 0.8 and 0.85) cathode material for lithium-ion batteries[J]. *J. Power Sources*, 2013, 233, 121–130.
- [9] Fleischhammer M, Waldmann T, Bisle G, Hogg B I, Wohlfahrt-Mehrens M. Interaction of cyclic ageing at high-rate and low temperatures and safety in lithium-ion batteries[J]. *J. Power Sources*, 2015, 274, 432–439.
- [10] Ren D, Hsu H, Li R, Feng X, Guo D, Han X, Lu L, He X, Gao S, Hou J, Li Y, Wang Y, Ouyang M. A comparative investigation of aging effects on thermal runaway behavior of lithium-ion batteries[J]. *eTransportation*, 2019, 2, 100034.
- [11] Liu T, Liu J, Li L et al. Origin of structural degradation in Li-rich layered oxide cathode[J]. *Nature*, 2022, 606, 305–312.
- [12] Sabet P S, Warnecke A J, Meier F, Witzhausen H, Laserna E M, Sauer D U. Non-invasive yet separate investigation of anode/cathode degradation of lithium-ion batteries (nickel-cobalt-manganese vs. graphite) due to accelerated aging[J]. *J. Power Sources*, 2022, 449, 227369.
- [13] Yang S, Hua Y, Qiao D, Lian Y, Pan Y, He Y. A coupled electrochemical-thermal-mechanical degradation modelling approach for lifetime assessment of lithium-ion batteries[J]. *Electrochim. Acta*, 2019, 326, 134928.
- [14] Wang Z, Wang J. An experimental investigation of the degradation and combustion behaviors associated with lithium ion batteries after different aging treatments[J]. *J. Clean. Prod.*, 2020, 272, 122708.
- [15] Fleischhammer M, Waldmann T, Bisle G, Hogg B I, Mehrens M W. Interaction of cyclic ageing at high-rate and low temperatures and safety in lithium-ion batteries[J]. *J. Power Sources*, 2015, 274, 432–439.
- [16] Abada S, Petit M, Lecocq A, Marlair G, Moynot V S, Huet F. Combined experimental and modeling approaches of the thermal runaway of fresh and aged lithium-ion batteries[J]. *J. Power Sources*, 2018, 399, 264–273.
- [17] Doyle M, Fuller T F and Newman J. Modeling of Galvanostatic Charge and Discharge of the Lithium/Polymer/Insertion Cell[J]. *J. Electrochem. Soc.*, 1993, 140, 1526.
- [18] Doyle M, Newman J. The use of mathematical modeling in the design of lithium/polymer battery systems[J]. *Electrochim. Acta*, 1995, 13-14(40), 2191–2196.
- [19] Ren H, Jia L, Dang C, et al. An electrochemical-thermal coupling model for heat generation analysis of prismatic lithium battery[J]. *Journal of Energy Storage*, 2022, 50: 104277.
- [20] He C, Yue Q, Wu M, et al. A 3D electrochemical-thermal coupled model for electrochemical and thermal analysis of pouch-type lithium-ion batteries[J]. *International Journal of Heat and Mass Transfer*, 2021, 181: 121855.
- [21] Zhang X, Shyy W, Marie Sastry A. Numerical simulation of intercalation induced stress in li-ion battery electrode particles[J]. *Journal of The Electrochemical Society*, 2007, 154(10): A910–A916.
- [22] Wu B, Lu W. Mechanical-electrochemical modeling of agglomerate particles in lithium-ion battery electrodes[J]. *Journal of The Electrochemical Society*, 2016, 163(14): A3131–A3139.
- [23] Ouyang D X, Weng J, Chen M, Wang J, Wang Z. Electrochemical and thermal features of aging lithium-ion batteries cycled at various current rates[J]. *J. Loss Prev. Proc.*, 2023, 85, 105156.
- [24] Sun B, Zhang C, Xu Z, Liu S, Yang Q. Ultrasonic diagnosis of the nonlinear aging characteristics of lithium-ion battery under high-rate discharge conditions[J]. *J. Power Sources*, 2023, 567, 232921.
- [25] Zhang G, Wei X, Chen S, Wei G, Zhu J, Wang X, Han G, Dai H. Research on the impact of high-temperature aging on the thermal safety of lithium-ion batteries[J]. *J. Energy Chem*, 2023, 87, 378–389.

- 1 [26] Yang R, Yu G, Wu Z, Lu T, Hu T, Liu F, Zhao H. Aging of lithium-ion  
2 battery separators during battery cycling[J]. *J. Energy Storage*, 2023, 63,  
3 107107.
- 4 [27] Zhang X, Li P, Wang K, Zhang H, Huang H. Numerical investigation on  
5 the elastoplastic behavior and fatigue life of the current collector of  
6 lithium-ion batteries based on the electrochemical-thermal-mechanical  
7 coupling model[J]. *J. Energy Storage*, 2023, 68, 107792.
- 8 [28] Luo P, Li P, Ma D, Wang K, Zhang H. Coupled Electrochemical-Thermal-  
9 Mechanical Modeling and Simulation of Lithium-Ion Batteries[J]. *J.*  
10 *Electrochem. Soc.*, 2022, 169(10), 100535.
- 11 [29] Yu R, Li P, Wang K, Zhang H. Numerical Investigation on the Impact of  
12 Linear Variation of Positive Electrode Porosity upon the Performance of  
13 Lithium-Ion Batteries[J]. *J. Electrochem. Soc.*, 2023, 170, 050502.
- 14 [30] Yin L, Borneklett A, Soderlund E, Brandell D. Analyzing and mitigating  
15 battery ageing by self-heating through a coupled thermal-electrochemical  
16 model of cylindrical Li-ion cells[J]. *J. Energy Storage*, 2021, 39, 102648.
- 17 [31] Wikner E. Division of Electric Power Engineering, Department of Electrical  
18 Engineering, Chalmers University of Technology, Göteborg, Sweden,  
19 2019.
- 20 [32] Luo P, Li P, Ma D, Wang K, Zhang H. A Novel Capacity Fade Model of  
21 Lithium-Ion Cells Considering the Influence of Stress[J]. *J. Electrochem.*  
22 *Soc.*, 2021, 168, 090537.
- 23 [33] Zhang X, Li P, Huang B, Zhang H. Numerical investigation on the thermal  
24 behavior of cylindrical lithium-ion batteries based on the electrochemical-  
25 thermal coupling model[J]. *Int. J. Heat Mass Transf.*, 2022, 199, 123449.
- 26 [34] Chen S C, Wan C C, Wang Y Y. Thermal analysis of lithium-ion  
27 batteries[J]. *J. Power Sources*, 2005, 140, 111.
- 28 [35] Wu B, Lu W. A battery model that fully couples mechanics and  
29 electrochemistry at both particle and electrode levels by incorporation of  
30 particle interaction[J]. *J. Power Sources*, 2017, 360, 360-372.
- 31 [36] Keil J, Jossen A. Electrochemical Modeling of Linear and Nonlinear Aging  
32 of Lithium-Ion Cells[J]. *J. Electrochem. Soc.*, 2020, 167, 110535.
- 33 [37] Yea Y, Shi Y, Cai N, Lee J, He X. Electro-thermal modeling and  
34 experimental validation for lithium ion battery[J]. *J. Power Sources*, 2012,  
35 199, 227–238.
- 36

# 基于电化学-热-力耦合模型的快速充电下锂离子电池的老化特性分析

左东旭, 李培超\*

(上海工程技术大学, 上海 201620)

**摘要:** 本文基于电化学-热-力 (ETM) 耦合模型, 对快速充电下锂离子电池 (LIB) 的老化特性进行了数值研究。首先, 通过 COMSOL Multiphysics 建立并求解了 ETM 耦合模型。随后, 对电池进行了长循环测试, 以探索 LIB 的老化特性。具体而言, 从 SEI 的非均匀分布、SEI 生长、热稳定性和应力特性等方面分析了充放电倍率和循环次数的增加对电池老化的影响。结果表明, 充放电倍率和循环的增加导致 SEI 不均匀程度的增加, 以及因 SEI 生成所造成的电池容量损失也随之增加。同时充放电倍率和循环数的增加也分别导致电池的发热量增加和散热率降低, 从而使得电极材料热稳定性下降。此外, 随着循环的进行, 正极材料的 von Mises 应力高于负极材料, 正极材料表现为拉伸变形, 负极材料表现为压缩变形, 正极的有效锂离子浓度低于负极的有效锂离子浓度, 证明了电池正极材料在长循环下所发生的拉伸型断裂主导了容量损失过程。上述研究有助于研究人员进一步探索锂离子电池在快速充电条件下的老化行为, 并采取相应的预防措施。

**关键词:** 锂离子电池; 老化特性; 快充; 电化学-热-力耦合模型;